ARTICLE

Extraspecific Manifestation of Nanoheater's Position Effect on Distinctive Cellular Photothermal Responses

Thang Do Cong, Zhimin Wang, Ming Hu, Qinyu Han, and Bengang Xing*

| Read Online

| ACCESS | | Metrics & More | | Article Recommendations | | SI Supporting Information |

ABSTRACT: Subcellular localization of nanoparticles plays critical roles in precision medicine that can facilitate an in-depth understanding of disease etiology and achieve accurate theranostic regulation *via* responding to the aiding stimuli. The photothermal effect is an extensively employed strategy that converts light into heat stimulation to induce localized disease ablation. Despite diverse manipulations that have been investigated in photothermal nanotheranostics, influences of nanoheaters' subcellular distribution and their molecular mechanism on cellular heat response remain elusive. Herein, we disclose the biological basis of distinguishable thermal effects at subcellular resolution by localizing photothermal upconversion nanoparticles into specific locations of cell compartments. Upon 808 nm light excitation, the lysosomal cellular uptake initialized by poly(ethylenimine)-modified nanoheaters promoted mitochondria apoptosis through the activation of Bid protein, whereas the cell surface nanoheaters anchored *via* metabolic glycol biosynthesis triggered necrosis by direct perturbation of the membrane structure. Intriguingly, these two different thermolyses revealed similar levels of heat shock protein expression in live cells. This study stipulates insights underlying the different subcellular positions of nanoparticles for the selective thermal response, which provides valuable perspectives on optimal precision nanomedicine.

KEYWORDS: upconversion nanoparticles, photothermal, NIR light, lanthanide, heat response
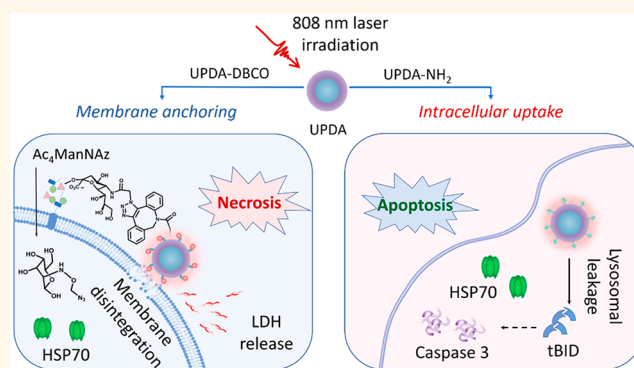
Within the three-dimensional cell structure, subcellular compartments have a substantial effect on locally activating signal transduction, trafficking essential components, and conveying biomolecules to manipulate cell events as well as downstream stress effectors.[1,2] Comprehension of how to specifically monitor organelle functions and to spatiotemporally regulate the unique signaling pathways in a sophisticated cell environment offers great possibility for an in-depth understanding of the etiology of disease procession. These conceptions can be fully employed for the facilitation of targeted theranostics with maximum efficacy.[3−9] Among the various endeavors for such high accuracy, the strategy based on light irradiations, especially utilizing the near-infrared (NIR) spectral window, represents an extraordinary option to achieve deep-tissue penetration and minimize side effects of ever-present biomolecules and endogenous chromophores.[10−13]

As one typical light-responsive therapeutic modality, photothermal treatment (PTT) directly utilizes the photoabsorbing components in nanostructures that are capable of absorbing

and converting photon energy to heat. Such light-transduced thermal effect can ablate targeted disease cells, thus engendering their promising applications in precision nanomedicine.[14−19] Thus far, a plethora of photothermal nanoabsorbers have been developed with a main focus on the strategies to improve biocompatibility, specific disease affinity, and photoconversion efficiency for maximal thermal regulation.[20−23] However, the biological basis conferring the cellular response to PTT is still controversial. In spite of the possibility of heat response through the expression of heat shock proteins (HSPs) as an intrinsic cytoprotective effect, their cochaperone interactions and molecular mechanism
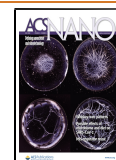
remain elusive.[24] Moreover, the cell death pathways including apoptosis or uncontrolled cell dying, namely, necrosis, occurring in the photothermal response to severe heat stress have also been intensively investigated but are mostly dependent on the temperature controls by the different light treatment settings including irradiation duration, laser type, and power intensity.[25,26]

Considering the importance of subcellular compartments in cell function mediations, organelle-specific localization of thermal-induced nanomaterials is critical for PTT precision with ultimate efficacy. Furthermore, attributed to the biological diversity in molecule components, native physiological properties and their relative proximity to heat sensors, subcellular compartments can be affected divergently by localized thermal stress, which might cause varied cellular responses.[27−29] However, despite the abundant designs of photothermal nanoheaters with significant efficiency, studies on their subcellular distribution and distinguishable effects on photothermolysis are still scarce.

Herein, we selected rare-earth upconversion nanoparticles with surface-coated polydopamine (termed UPDAs) as a representative model of tissue-penetrable NIR light-activated nanoheaters for dissecting intracellular behaviors to heat shock responses, mostly due to their unique photoluminescence properties.[30−35] Different intracellular recognition of UPDAs can be achieved by selective moderation of particles' surfaces with poly(ethylenimine) (PEI) and membrane-associated bioorthogonal moieties. Typically, UPDAs were coated with PEI to provide enhanced cell uptake for efficient cytoplasm localization. We incorporated a monosaccharide precursor, peracetylated N-azidoacetylmannosamine (Ac$_4$ManNAz), modified with a bioorthogonal azido tag, N$_3$, on the cell surface through the process of intrinsic glycan metabolism. Meanwhile, nanoparticles functionalized with DBCO (dibenzyl cyclooctyne) were conjugated with the pretreated N$_3$-tagged glycans *via* copper-free click reaction, achieving specific surface localization of UPDAs onto live cells.[10] Upon 808 nm laser excitation, heat released from specifically localized UPDAs was monitored to comparatively study the heat shock response in cells, thus disclosing their molecular modes of cell death (Scheme 1).

RESULTS AND DISCUSSION

Rational Designs and Characterizations of Upconversion Nanoheaters. Figure 1A presents the design of our

Scheme 1. Specific localization of photothermal upconversion nanoparticles reveals distinguished cellular responses to heat stress.
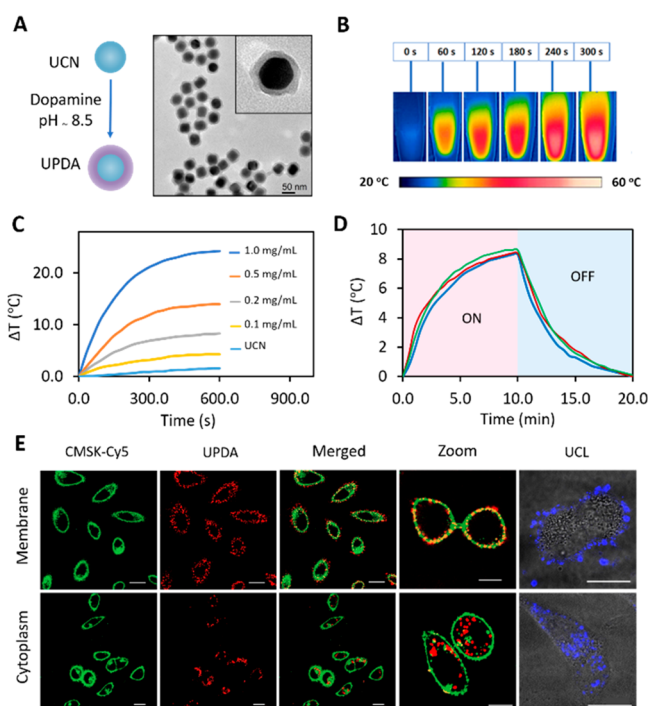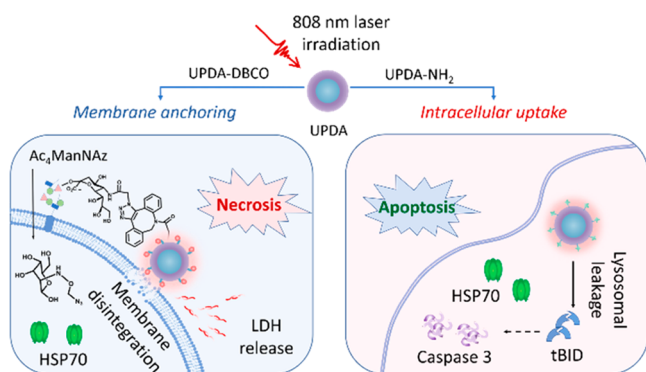
Figure 1. Fabrication and characterization of nanoheaters and specific localization in cells. (A) Polydopamine coating scheme and TEM image of polydopamine coated on upconversion nanoparticles. (B) Thermal images of irradiation-time-dependent temperature increase (1 mg/mL UPDA) in aqueous solution. (C) Temperature curves of UPDAs under different concentrations upon 808 nm irradiation for 10 min (1.3 W/cm^2), with UCNs without surface coating as a control. (D) Heating curves of UPDA, UPDA-NH$_2$, and UPDA-DBCO (200 μg/mL) during laser irradiation and natural cooling process. (E) Confocal fluorescence and upconversion luminescence (UCL) of membrane conjugation of UPDA-DBCO (top) and cytoplasm distribution of UPDA-NH$_2$ (down). Green: CMSK-Cy5 (λ_{ex}: 640 nm, λ_{em}: 670/50 nm), red: UPDAs (λ_{ex}: 543 nm, λ_{em}: 580/50 nm), UCL imaging at λ_{em} 460/50 nm. Scale bar: 20 μm.

NIR light-responsive nanoheaters, in which biocompatible polydopamines with high NIR spectral absorbance[36] were coated on lanthanide-doped upconversion nanoparticles (UCNs) to produce a promising photothermal effect after 808 nm laser excitation. Transmission electron microscope (TEM) images show the homogeneous coating of polydopamine on UCNs with a thickness of 8 nm (Figure 1A). The hydrodynamic diameter in buffer solution was determined as 100.5 ± 19.13 nm through dynamic light scattering (DLS) analysis (Figure S1A). Meanwhile, upconversion luminescence characterized by blue emission peaked at 460 nm facilitates the applicable tracking of UPDA position in live cells (Figure S1B). We then modified UPDAs with different chemical moieties, *e.g.*, DBCO and PEI, on the particle surface (Figure S1C). The successful conjugation of DBCO on UPDA and effective click chemistry with the N$_3$ group was confirmed by the fluorescent conjugation through 5-carboxyfluorescein-azide (FAM-N$_3$) with the optimal amount of DBCO of ∼363 nmol/ mg (Figure S2). Moreover, PEI was coated on UPDA for increasing the efficiency of cellular uptake, which further enhanced the subsequent localization in the cytoplasm. There was no obvious morphology and shape difference observed among the modified nanoparticles (Figure S1D,E). Zeta potential measurement indicates a negative value of −10 mV

for UPDA-DBCO, while a positive potential was found for UPDA-NH$_2$ (+16 mV) (Figure S1F), indicating its great possibility for cell uptake.

The obtained nanoheaters demonstrated time- and concentration-dependent heat effects (Figure 1B,C) upon 808 nm light illumination, which was also observed even under deep tissue depth (Figure S19). Importantly, the UPDAs showed great stability in different pH conditions (Figures S3 and S4) and repeated cycles of photothermal treatment (Figure S5). Moreover, these particles indicated similarity in heating and natural cooling cycles in their photothermal performance (Figure 1D) and were calculated to have comparable photothermal conversion efficiencies (Figure S6). These properties enable a reasonable comparison of heat response through different localization of UPDAs in cells by introducing an equal amount of nanoparticles in each position of interest.

Specific Cellular Localization of Nanoheaters. For conjugation of nanoparticles on the cell membrane, the covalent glycan labeling approach was first conducted by introducing the N$_3$-tagged glycans onto human lung adenocarcinoma epithelial (A549) cells. Upon feeding with Ac$_4$ManNAz precursor (50 μM) for 48 h, the A549 cells were incorporated with azido groups on the membranes through ubiquitous cellular metabolism (Figure S7). The N$_3$-tagged cells were further incubated with UPDA-DBCO, and dynamic imaging was performed, revealing the gradual localization of UPDA on the cell membrane (Figure S8). The membrane accumulation of nanoparticles reached a plateau after 1 h. Notably, an extended incubation time (e.g., 2 h) resulted in slow cellular internalization, while the majority of UPDAs were still anchored on the cell membrane. Moreover, control studies by unmodified UPDAs alone or untagged cells revealed a negligible number of nanoparticles on the cell surface, which further consolidated the specificity of the labeling through the metabolic glycol biosynthesis (Figure S9). During this process, care needs to be taken to maximize the quantity of UPDA on the cell surface with minimum internalization by optimizing the incubation time (e.g., 1 h) to make sure that the specific thermal response mainly originates from the membrane-localized nanoheaters (Figure S8).

In addition, we examined the possibility for different localizations of upconversion nanoheaters in live cells. Typically, the effective cellular distribution of nanoparticles inside cells can be obtained by incubation of A549 cells with UPDA-NH$_2$. The time-dependent cellular uptake was monitored by confocal and upconversion imaging analysis to optimize the comparable quantity of nanoparticles internalized in contrast to those UPDA-DBCO counterparts located on the membrane upon proper time incubation (e.g., 6 h, Figure S10). Indeed, as shown in Figure 1E, different from the UPDA-DBCO labeled on the plasma membrane, the UPDA-NH$_2$ could be taken up efficiently, and almost no membrane-located interference was observed in cell imaging. In order to monitor their contribution to the cellular thermal response, we individually localized UPDA-DBCO and UPDA-NH$_2$ into different compartments and then carried out ICP measurement to quantify the amount of incubated UPDA in live cells.[37,38] The relatively same number of nanoabsorbers (e.g., a ratio of ~1:1.05) were precisely maintained on the cell membrane and cytoplasm, respectively (Figure S11), which promises a rational strategy for further comparative investigations.

Heat Shock Protein Expression upon Photothermal Stimulation. Upon the localization of UPDAs on the different positions in the cells, both the nanoheaters on the membrane and in the cytoplasm were irradiated with an 808 nm laser (1.3 W/cm^2) for thermolysis analysis. The heat effect was carefully monitored through the NIR thermograph to optimize the proper concentration (e.g., 200 μg/mL) and temperature increment (e.g., ~ 8.5 °C) (Figures 1C, S12) for an effective photothermal response in live cells.[39] Prior to NIR light irradiation, there was no obvious thermolysis observed in the nanoparticles localized on cells without laser illumination, suggesting negligible cell perturbation even under a high concentration of nanoparticles (Figure S12A). After laser irradiation, cells with specific UPDA localization experienced a significant thermolysis effect (Figure S12B), suggesting a suitable concentration and light treatment for further photothermal study.

Notably, soon after being subjected to the heat stress, the cells started to produce heat shock protein, as a cytoprotective response against the detrimental increase of temperature (Figure S13).[40] Three hours after the heat stress triggered by NIR laser irradiation, both groups of cells with different subcellular nanoheater localization showed a significant production of HSP70, as indicated by green fluorescence from Alexa Fluor 488 labeled anti-Hsp70 antibody (Figure 2A,B). Controlled experiments showed the minimum expression of HSP70 in cells that lack UPDA treatment or without laser irradiation (Figure S14). Quantitative fluorescence-activated cell sorting (FACS) analysis demonstrated a relatively equal amount of HSP70 expression at both 1 and 3 h postirradiation in each group of cells (Figure 2D,E,F).
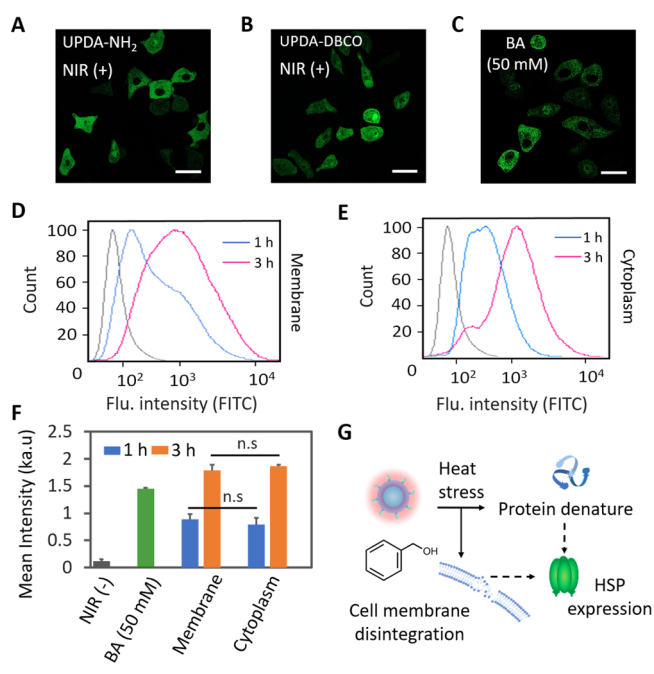

Figure 2. Cellular analysis of photothermal effect and heat shock response. (A) Confocal images of HSP70 expression in A549 cells treated with localized UPDA-NH$_2$, (B) UPDA-DBCO, 3 h after photothermal stimulation, and (C) benzyl alcohol (50 mM). Scale bar in images: 40 μm (λ_{ex}: 488 nm, λ_{em}: 515/30 nm). (D, E) Flow cytometry analysis of HSP70 expression at different time points postirradiation of cells with membrane- and cytoplasm-localized UPDAs, respectively. Treated cells were stained with Alexa Fluor 488 labeled anti-Hsp70 antibody. (F) Mean intensity of HSP70 levels. (G) Potential mechanism of heat shock protein expression.

Although the detailed mechanism of such stimulated protection remains controversial, the heat-induced native protein denaturation could be a possible driving force to stimulate the transcription of heat shock proteins upon binding to the promotor of the specific HSP gene.[41] Additionally, recent studies also indicated the possibility of membrane perturbation for cytoprotective HSP70 expression, in which cell surface disruption could compromise the membrane integrity and give rise to bulky membrane hyperfluidization.[42] To this end, we treated the live cells with benzyl alcohol (BA), a typical membrane perturbation reagent. Indeed, as shown in Figure 2C, the effective activation of HSP70 clearly suggested the possible involvement of membrane function and the integrity in cellular response to the stimulated stress. In our case, the accumulation of UPDA on the membrane concentrated heat onto a confined area, which possesses low thermal conductivity and may therefore contribute to larger temperature gradients and membrane disruption.[43,44] Apparently, UPDA membrane conjugated A549 cells indicated a well-organized surface structure with a specific residing of nanoparticles before NIR light exposure. However, 15 min after laser irradiation, the membrane tracker signal was disturbed, and the signal showed the release of cytoplasm components after 30 min (Figure S15). These results confirmed the occurrence of membrane perturbation during stimulation of UPDAs localized on the cell surface. Although the detailed processes involving HSP expression require further investigation, the potential disruption of membrane integrity triggered by heat stimulation would be one noticeable perspective (Figure 2G).

Distinguishable Photothermolysis at Different Subcellular Locations. We further examined the possible mode of cell death after NIR irradiation of nanoheaters located in different cellular compartments. Typically, cells with site-specific labeling of UPDAs were irradiated, and the standard annexinV/propidium iodide (AnnV/PI) costaining was recruited to compare the cell death pathways. As shown in Figure 3A, heat from cytoplasm-located UPDAs stimulates outer membrane translocation of phosphatidylserine (PS) at early time points after irradiation, as detected by green emission from the FITC-AnnV binding protein. Upon further incubation, PI molecules gradually permeated into the nucleus. In contrast, cells with membrane-conjugated UPDAs experienced rapid intracellular uptake of PI molecules. Moreover, the levels of apoptosis and necrosis were analyzed by FACS. Figures 3B and S16 show consistent results as observed from confocal imaging. Particularly, at 1 and 3 h postirradiation, cells that internalized the UPDA encountered 4.96% and 16.12% early apoptosis, respectively. This group of cells faced secondary necrosis with approximately 31.15% of total cells after 5 h of incubation. Meanwhile, the membrane-localized UPDA induced a gradual increase in necrosis level from the initial stage after illumination (4.48% in 1 h to 47.09% after 5 h), and a minimum amount of early apoptosis was detected. Such different thermal response revealed that UPDA-internalizing cells experienced the apoptotic process and retained membrane integrity at the primary stage after illumination. In contrast, membrane-localized UPDAs obviously caused membrane perturbation, which allows prompt internalization of PI molecules, and therefore likely progress the cell death pathway to necrosis.

To further validate the distinguished cellular lethality, the molecular basis associated with light-triggered thermolysis was
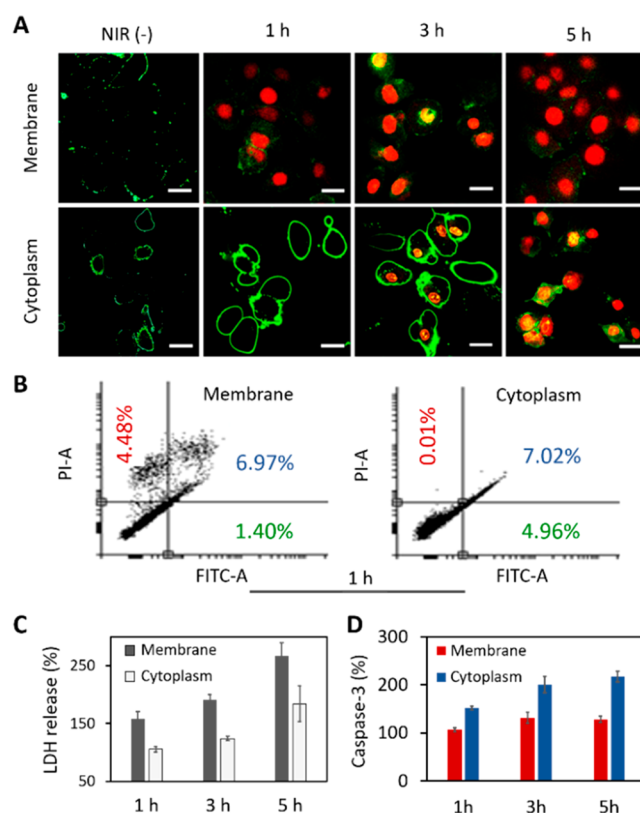

Figure 3. Cell death pathway analysis. (A) Confocal images of AnnV-PI costaining of the cells with specific nanoheater localization after heat stress. Green: FITC (λ_{ex}: 488 nm, λ_{em}: 515/30 nm), red: PI (λ_{ex}: 543 nm, λ_{em}: 580/50 nm). Scale bar: 20 μm. (B) FACS analysis of apoptosis and necrosis by AnnV-PI staining of different groups of cells at 1 h after irradiation. (C) LDH release and (D) caspase 3 activity at 1, 3, and 5 h after laser irradiation of cells with the UPDAs on the membrane and in the cytoplasm.

investigated. First, we employed lactate dehydrogenase (LDH) leakage as an indicative assay for membrane integrity. As indicated in Figure 3C, irradiation of cell surface distributed UPDAs could lead to a time-dependent LDH release. Specifically, at 5 h postirradiation, there was nearly a 3 times increase in LDH level as compared to the initial amount observed in the same culture medium. Differently, LDH content in the medium was found to rise slightly in cytoplasm-localizing UPDAs, and the rate of leakage was much slower than the former case of UPDAs on the cell surface. These different outcomes further confirmed the presence of necrosis in cells with membrane-located UPDAs.

Second, we investigated the activation of caspase 3, a standard biomarker for apoptosis, after locally triggered heat stress by NIR light irradiation. The fluorescent signal from caspase 3 probes was analyzed to monitor caspase 3 expression. As shown in Figure 3D, the level of caspase 3 enzyme in live cells with cytoplasm accumulation of nanoheaters rose to around 2 times within 3 h after laser irradiation, whereas in cells with particles conjugated on the plasma membrane, less enzyme expression was detected even after prolonging the incubation time, up to 5 h after laser irradiation.

So far, apoptosis has well been recognized as a standard pathway in heat-stimulated cell death, and lysosomal leakage of nanoheaters would be a critical step that initiates a chain of events before activating caspase 3 in apoptosis (Figure

4A).[45,46] Such initial step of cell death was also observed in our cells with cytoplasmic UPDA localization under NIR light
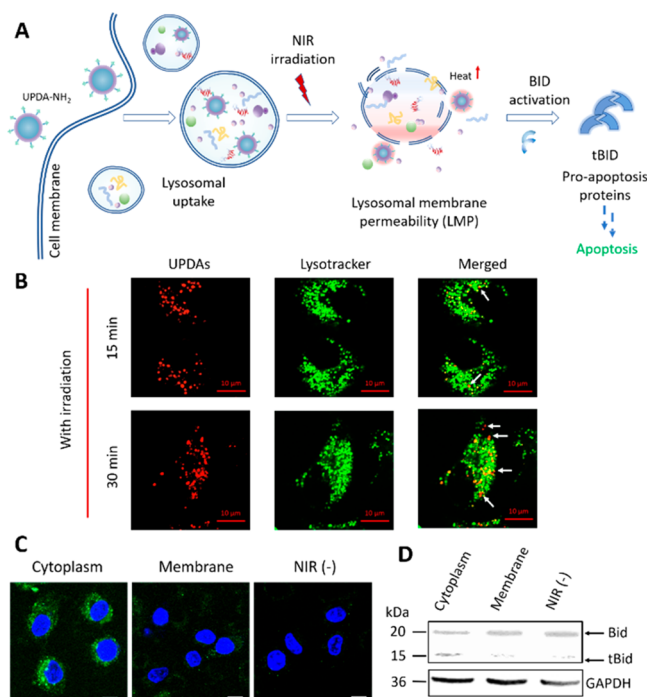

Figure 4. Lysosomal permeability to activate the pro-apoptosis protein. (A) Scheme of lysosomal leakage induced apoptotic cell death. **(B)** Confocal images indicating lysosomal escape of UPDA-NH$_2$ at 15 and 30 min after 10 min of 808 nm irradiation (1.3 W cm^{-2}). White arrows indicate location of UPDA-NH$_2$ after lysosomal release. Green: Lysosomal tracker, Alexa Fluor 488 (λ_{ex}: 488 nm, λ_{em}: 515/30 nm), red: UPDA (λ_{ex}: 543 nm, λ_{em}: 580/50 nm). **(C)** Images of tBID expression in cells with site-specific nanoparticle localization at 5 h postirradiation. Blue: Hoechst 33342 (λ_{ex}: 405 nm, λ_{em}: 460/50 nm), green: Alexa Fluor 488 (λ_{ex}: 488 nm, λ_{em}: 515/30 nm). Scale bar: 20 μm. **(D)** Western blot analysis of Bid activation after irradiating the site-specific located UPDA. GAPDH was used as internal control.

exposure. After being internalized, UPDAs were mostly loaded in the lysosome, as confirmed by colocalization of lysosome tracker (green) and UPDA (red) with the yellow color in the merged image (Figure S17). Nanoparticles were released from the lysosome, presenting as a single red color signal after 10 min of NIR light illumination, while negligible lysosomal escape was observed in the cells without laser irradiation (Figures 4B, S18). Principally, heat stress from nanoheaters disrupts the integrity of the lysosomal membranes, resulting in lysosomal membrane permeability that triggers the cathepsin-mediated cell death pathway. At an early stage of this process, a pro-apoptotic protein, Bid, can be cleaved to its truncated tBid form and initialize the intrinsic mitochondria apoptosis pathway.[47] Herein, we evaluated the level of tBid in two groups of cells with site-specific localization of UPDA on the membrane and in the cytoplasm, respectively. Typically, immunofluorescence analysis exploiting tBid antibody and fluorescent secondary antibody was applied to label the tBid protein. As indicated in Figure 4C, tBid was activated in cytoplasmic UPDA containing cells, revealed by the green fluorescence, while the membrane-accumulated one showed lower intensity. A Western blot experiment was also performed, and the results clearly indicated the decreased

amount of the full-length Bid and the enhanced quantity of tBid in the UPDA-internalizing cells in response to photothermal stress. Meanwhile, the similar irradiation of cells with membrane-located UPDAs resulted in an insignificant tBid expression in comparison with the control without laser treatment (Figure 4D). These distinctive observations demonstrated that the localization of UPDAs in lysosome organelles and their subsequent liberation can convert the Bid protein to its activated form, tBid, which thus functions as a key factor to initialize apoptosis. These fundamental biological assays clearly indicated the importance of the subcellular position of nanostimulators for their differentiated heat response, which will therefore affect further cell lethality significantly.

CONCLUSION

In summary, NIR light responsive upconversion nanoheaters positioned at different cellular locations can differently affect the process of cell responses upon photothermal stress. On one hand, we employed the intrinsic glycan metabolic process to introduce the azido group on the cell surface, which subsequently conjugated the DBCO-modified UPDAs onto the cell membrane. Upon 808 nm laser irradiation, temperature elevation caused by UPDA-DBCO promoted the destruction of the plasma membrane, thus stimulating the expression of HSP70 and directing the cell death to necrosis. In contrast, UPDA-NH$_2$ were internalized by cells, where these cytoplasm-localized nanoparticles not only induced HSP70 expression upon light-triggered temperature increment as those UPDAs on the cell surface but, more significantly, can also promote lysosomal membrane permeability upon photothermal treatment, thereby inducing the activation of tBid cleavage and resulting in a differentiated cell death, apoptosis. Our study specifically revealed the molecular basis of the critical importance of photothermal nanoparticles with organelle-specific localization in manipulating cellular responses. With the ubiquitous properties of these organelles responsible for multiple cellular pathways, we expect that the integration with innovative nanotechnology designs could offer great opportunity to precisely regulate other cell functions and better understand the cellular basis of photothermal responses. Prospectively, this strategy could render optimized practical conditions for future personalized nanomedicine.

EXPERIMENTAL PROCEDURES

Materials. Y(CH$_3$CO$_2$)$_3$, Yb(CH$_3$CO$_2$)$_3$, Tm(CH$_3$CO$_2$)$_3$, Nd-(CH$_3$CO$_2$)$_3$, oleic acid, 1-octadecene, NH$_4$F, NaOH, peracetylated *N*-azidoacetylmannosamine, *in vitro* toxicology assay kit (TOX8, resazurin based), Hoechst 33342 (bisbenzimide H 33342 trihydrochloride), dibenzylcyclootyne-amine (DBCO-NH$_2$), DBCO-Cy3, 5-carboxyfluorescein-azide (FAM-N$_3$), dopamine hydrocloride, branched polyethylenimine (PEI$_{25000}$), annexin V−PI detection kit, and caspase-3 fluorometric assay kit were purchased from Sigma-Aldrich. The CytoTox 96 nonradioactive cytotoxicity assay kit was purchased from Promega. Rabbit monoclonal [Y8] to Bid and goat anti-rabbit IgG H&L (Alexa Fluor 488) were purchased from Abcam. BID p15 polyclonal antibody was purchased from Thermo Fisher. Dulbecco's modified Eagle medium (DMEM), minimum essential medium (MEM), fetal bovine serum (FBS), penicillin−streptomycin, trypsin−EDTA, and Cell Mask deep red plasma membrane stain kit (CMSK-Cy5) were used. All the commercial reagents were used as received unless otherwise noted. The human lung adenocarcinoma epithelial cell line (A549) was cultured in DMEM with 10% FBS at 37 °C in a humidified atmosphere with 5% CO$_2$.

Characterization and Measurement. TEM images were obtained using a FEI EM208S TEM (Philips) operated at 100 kV. DLS and zeta potential measurements were performed by a Brookhaven 90 Plus nanoparticle size analyzer. Fluorescence emission spectra were recorded on an RF-5301PC spectrofluorophotometer (Shimadzu, Japan) at room temperature. Photothermal performance was monitored by an FLIR E60 thermal imaging camera. The cell viabilities were measured by a Tecan Infinite M200 microplate reader. Confocal imaging of cells was carried out on a Carl Zeiss LSM 800 confocal laser microscope (Germany). Photoirradiation experiments were performed with an 808 nm NIR diode laser (Changchun New Industries Optoelectronics Technology Co., Ltd., China). Flow cytometry analysis was performed using a BD LSRFortessa X-20 flow cytometer.

Synthesis of PDA-Coated UCNPs (UPDAs). The synthesis of $NaYF_4$:Yb/Tm/Nd (30/0.5/1%) @$NaYF_4$:Nd (20%) core−shell upconversion nanoparticles was based on the standard method published by our group previously.[10] Subsequently, in a flask containing 5 mL of cyclohexane and 5 mg of the prepared core−shell UCNs, 0.4 mL of Igepal CO-520 was added and sonicated for 30 min. Then, 40 μL (28 wt % in water) of ammonium hydroxide was carefully added into the solution and stirred for 30 min. The aqueous solution of dopamine hydrochloride was prepared from 16 mg of dopamine hydrochloride in 100 μL of deionized water (for an 8 nm polydopamine shell thickness) before slow addition of the above mixture under ultrasonication at a rate of 5 μL min^{-1}. The reaction mixture was stirred for an additional 24 h. The UPDAs were precipitated by adding ethanol, collected by centrifugation, and washed several times with ethanol and water.

Synthesis of UPDA-DBCO, UPDA-NH$_2$, and Rhodamine-UPDA. The polydopamine-coated UCNs were covalently modified with DBCO-NH$_2$ by typical Michael addition and/or Schiff-based reaction with catechol and amine groups on the UPDAs. Briefly, the as-prepared UPDAs (5 mg) were dissolved in Tris buffer solution (pH 8.5) with a mixture of deionized water and ethanol (2:1) as solvent. DBCO-NH$_2$ (5 mg) was dissolved in ethanol before carefully added into the prepared mixture. After 24 h of magnetic stirring at room temperature, DBCO-UPDA was obtained by centrifugation (14 000 rpm, 10 min) and washed by ethanol three times to remove excess reactant. The precipitate was stored in a fridge before use. The amount of DBCO moiety on the surface of UCNs was determined based on the fluorescence of conjugated FAM-N$_3$ molecules by copper-free click chemistry reaction. Generally, the as-prepared DBCO-UPDA (1 mg) were dissolved in DMSO (200 uL) containing FAM-N$_3$ (0.2 mg, 43.6 μmol) and stirred in the dark for 2 h. The nanoparticles were centrifuged (14 000 rpm, 10 min) and washed by ethanol three times to remove excess reactant. The precipitate was redispersed in 1 mL of DMSO for later determination of the DBCO binding efficiency by measuring the fluorescence at 540 nm, excitation: 488 nm.

The synthesis of UPDA-NH$_2$ was conducted by dispersing the UPDAs (5 mg) in a 1 mg/mL branched polyethylenimine (PEI$_{25000}$) solution and stirring for 12 h. The obtained UDPA-NH$_2$ was collected by centrifugation (14 000 rpm, 10 min) and washed with ethanol and water.

For UPDAs to be tracked from confocal imaging, rhodamine B-UPDAs were synthesized. Specifically, 1 mg of rhodamine B was activated by EDC/NHS (1:1 molar ratio) in DMSO at room temperature for 2 h. The mixture was then added dropwise into the UPDA aqueous solution (5 mg of UPDA) and stirred vigorously overnight. The obtained nanoparticles were collected by centrifuging (14 000 rpm, 10 min) and washed with ethanol three times to remove unbound dyes.

Photothermal Performance Measurement. A 0.2 mL aqueous dispersion of different concentrations of UPDA nanocomposites was irradiated with an 808 nm laser at 1.3 W cm^{-2} for 10 min, and the temperature changes were monitored by an infrared thermal camera (E60, FLIR).

Cell Membrane Conjugation of DBCO-Functionalized Agents. The human lung adenocarcinoma epithelial (A549) cell line were cultured in DMEM supplemented with 10% FBS, 100 units mL^{-1} penicillin, and 100 μg mL^{-1} streptomycin and maintained in a humidified incubator with 5% CO$_2$ at 37 °C. The cells were subsequently incubated with a density of 5×10^5 cells in an ibidi dish (35 mm, plastic bottom) in 1 mL of DMEM medium with Ac$_4$ManNAz (50 μM) for 48 h. The resulting azido-labeled cell membrane was then stained with DBCO-Cy3 (10 μM, 30 min), CMSK-Cy5 (5 μM, 10 min), and Hoechst 33342 (1 μM, 30 min) separately. The cells without azido sugar treatment and azido-labeled cell membrane blocked with DBCO-NH$_2$ (50 μM, 30 min) were used as control experiments.

Conjugation of UPDA-DBCO on the Cell Membrane. A total of 5×10^5 A549 cells were cultured in an ibidi dish (35 mm, plastic bottom) and incubated with Ac$_4$ManNAz (50 μM) in DMEM at 37 °C, 5% CO$_2$ for 48 h. The cells were then washed with PBS (pH 7.4) three times before adding 200 μg/mL of UPDA-DBCO in 1 mL of DMEM. After a further 1 h incubation, the cells were washed carefully with PBS three times and the specific localization of nanoparticles was monitored by a confocal microscope with CMSK-Cy5 as a membrane tracker.

UPDA-NH$_2$ Localization in the Cytoplasm. A total of 5×10^5 A549 cells were cultured in an ibidi dish (35 mm, plastic bottom) in DMEM. After 48 h, the cells were washed with PBS three times before adding 200 μg/mL UPDA-NH$_2$ and further incubated for 6 h. The specific distribution of nanoparticles inside the cells was monitored using a confocal microscope with CMSK-Cy5 as a membrane tracker.

ICP Quantification of UPDA. Two groups of cells after specific localization of UPDAs (using optimized conditions for each localization) were washed three times with PBS. After that, the cells were collected by 0.25% trypsin−EDTA, centrifuged at high speed (10 000 rpm, 10 min), and treated with 70% nitric acid for 24 h. The clear solution was diluted in water (2% nitric acid), filtered with a 0.22 μm filter, and analyzed for yttrium (Y^{3+}) concentration by ICP-OES.[37,38]

Cell Viability Test. The A549 cells were seeded with a density of 1×10^4 cells per well in 200 μL of DMEM in the 96-well plate and incubated with 50 μM Ac$_4$ManNAz for another 48 h before adding UPDA-DBCO with different concentrations in 1 h for membrane conjugation and incubated for 24 h. Meanwhile, other A549 cells were seeded with a density of 1×10^4 cells per well in 200 μL of DMEM in the 96-well plate and incubated for 48 h before washing carefully with PBS and incubating with different concentrations of UPDA-NH$_2$ in culture medium for internalization during 24 h. After that, the cells treated with different nanoparticles were washed with PBS, fresh cell culture medium containing TOX8 was added to the wells, and the plate was incubated for another 3 h. The fluorescence at 590 nm was measured by a Tecan Infinite M200 microplate reader with 560 nm excitation. Cell viability was expressed by the ratio of the fluorescence of cells conjugated with nanoparticles to that of the control.

For photothermal cell viability test, A549 cells with specific conjugation of UPDAs were monitored with previously mentioned incubation times to have equal numbers of nanoparticles in each group of cells before being irradiated with a 1.3 W cm^{-2} 808 nm laser for 10 min. The photothermally treated cells were then further incubated for 24 h before being washed with PBS, and the viability was measured using the same TOX8-based method described above.

Hsp70 Expression Analysis. A549 cells with membrane-conjugated and cytoplasm-localized UPDAs were seeded on eight-well ibidi dishes containing 5×10^4 cells per well in 200 μL of DMEM media. After 10 min of irradiation with 1.3 W cm^{-2} 808 nm laser irradiation with additional incubation for 5 min, 1 h, 3 h, and 5 h, A549 cells were washed and fixed with 4% paraformaldehyde solution for 15 min at room temperature. After that A549 cells were washed with PBS before staining with anti-Hsp70 antibody conjugated with Alexa Fluor 488 (Biolegend Alexa Fluor 488 anti-Hsp70) at room temperature for 15 min. Stained A549 cells were washed with PBS and observed with a confocal microscope.

For flow cytometry (FCM) analysis, A549 cells were seeded in six-well dishes in 2 mL of DMEM cell culture media with a density of $1 \times$

10^6 cells per well, and site-specific localization of UPDA-DBCO and UPDA-NH$_2$ (200 μg/mL for each) was allowed . After photothermal treatment as in the above-mentioned method, cells were further incubated for 1 or 3 h before being collected by 0.25% trypsin-EDTA and fixed with 4% paraformaldehyde solution for 15 min at room temperature. The collected cells of each groups were washed with PBS before staining with anti-Hsp70 antibody conjugated with Alexa Fluor 488 (Biolegend Alexa Fluor 488 anti-Hsp70) at room temperature for 15 min. Stained A549 cells were washed with PBS and analyzed with a BD LSRFortessa X-20 flow cytometer.

For benzyl alcohol induced HSP70 expression, 1×10^6 cells in ibidi dishes (35 mm) were incubated with 50 mM BA in cell culture DMEM for 1 h. After that, the cells were carefully washed with PBS and fixed with 4% paraformaldehyde solution for 15 min at room temperature before staining with anti-Hsp70 antibody conjugated with Alexa Fluor 488 (Biolegend Alexa Fluor 488 anti-Hsp70) at room temperature for 15 min. Stained A549 cells were washed with PBS and observed with a confocal microscope, using a 488 nm laser and a 480 ± 25 nm filter. For FCM analysis, cells with the same BA treatment condition were collected by 0.25% trypsin-EDTA and fixed with 4% paraformaldehyde solution for 15 min at room temperature. The collected cells were then washed and stained with anti-Hsp70 antibody before being analyzed with a BD LSRFortessa X-20 flow cytometer.

Apoptosis/Necrosis Imaging and FCM Analysis. A double-staining molecular probe consisting of AnnV for detecting apoptotic cells and PI staining of necrotic cells was used to investigate the membrane integrity as well as cell necrosis and apoptosis. Typically, a 5 μL volume of AnnV (100 μg/mL) and a 1 μL volume of PI (100 μg/mL) were added to each group of cells with different site-specific UPDA localization after photothermal treatment in 100 μL of 1× annexin-binding buffer. After staining, fluorescence images were taken using a Carl Zeiss LSM 800 confocal laser microscope, and the quantity of early apoptotic, late apoptotic, and necrotic cells was analyzed by a BD LSRFortessa X-20 flow cytometer.

LDH Release Assay. For investigation of necrosis, the Cyto Tox 96 assay (Promega) was carried out according to the manufacturer's instructions. Generally, each group of site-specific UPDA localization cells was grown in a 96-well plate with a 1×10^4 cells/well density. Cells was washed with PBS before photothermal treatment. After 1, 3, and 5 h of additional incubation, the sample solution was incubated with LDH substrate buffer solution in the dark for 30 min. Then, stop solution was added before measuring the absorbance at 490 nm on a Tecan Infinite M200 microplate reader. Each experiment was repeated three times, and the results were reported in average values and standard deviations.

Caspase 3 Activity Assay. The caspase 3 activity assay (caspase 3 assay kit, fluorimetric, Sigma-Aldrich) was carried out according to the manufacturer's instructions. Typically, 1×10^4 site-specific UPDA localization cells were grown in each well of a 96-well plate. After photothermal treatment, cells were washed with PBS, and lysis buffer was added. The cells were then lysed at 0 °C for 20 min. Then, assay buffer containing caspase 3 probe was added and further incubated for 30 min. The increase in fluorescence at 460 nm under 360 nm excitation of each sample solution was recorded by a Varian Cary Eclipse fluorescence spectrophotometer. Each experiment was repeated three times, and the results were reported as average values and standard deviations.

Immunofluorescence Analysis of tBid Protein. Each group of cells with site-specific localization of UPDAs with a density of 5×10^4 cells in each well of eight-well ibidi dishes experienced photothermal treatment as described above. After 5 h further incubation, the cells were fixed with 4% paraformaldehyde for 15 min, permeabilized with 0.25% Triton X-100 for 10 min, and blocked with 5% BSA for 1 h at room temperature. The cells were then labeled with BID (p15) Rabbit polyclonal Antibody in 1% bovine serum albumin (BSA) and incubated for 3 h at room temperature. Subsequently, Alexa Fluor 488-goat anti-rabbit IgG secondary antibody was stained for 30 min at room temperature. The nucleus was stained with Hoechst 33342. The induction of the Bid cleavage site (p15 tBID) was visualized with a

Carl Zeiss LSM 800 microscope (Hoechst 33342: Ex = 405 nm, Em = 460/50 nm; Alexa Fluor 488: Ex = 488 nm, Em = 515/30 nm).

Western Blot Analysis of Bid Protein Activation. The lysates of each group of cells with site-specific-localized UPDAs at 5 h after photothermal treatment were collected and centrifuged at 12000g for 10 min at 4 °C. Protein levels in supernatants were determined using Nanodrop and equalized to the same concentration and boiled for 10 min with SDS-PAGE sample loading buffer before being separated using SDS-PAGE and transferred to the PVDF membrane. The membrane was then blocked with 5% BSA-TBST blocking buffer overnight at 4 °C. Subsequently, full-length BID primary antibody (1:2000) (rabbit monoclonal [Y8] to Bid, Abcam) and p15 Bid cleavage site-specific antibody (1:1000) were incubated at room temperature for 2 h in 2% BSA−TBST buffer. After a series of washings, the goat-anti rabbit IGG (H&L) secondary antibody was added and incubated for 1 h in 2% BSA−TBST. All signals were developed using a Super Signal West Femto kit, visualized using a myECL imager.

ASSOCIATED CONTENT

Ⓢ Supporting Information

The Supporting Information is available free of charge at https://pubs.acs.org/doi/10.1021/acsnano.0c00951.

> Further characterization of nanoparticles (TEM, DLS, stability tests, photothermal conversion efficiency); optimized treatment conditions of nanoparticles to achieve specific cell compartment localizations; further details and control experiments of heat shock responses and cell death mechanism (PDF)

AUTHOR INFORMATION

Corresponding Author

Bengang Xing − *Division of Chemistry and Biological Chemistry, School of Physical & Mathematical Sciences, Nanyang Technological University, Singapore 637371 Singapore;* ⓘ orcid.org/0000-0002-8391-1234; Email: Bengang@ntu.edu.sg

Authors

Thang Do Cong − *Division of Chemistry and Biological Chemistry, School of Physical & Mathematical Sciences, Nanyang Technological University, Singapore 637371 Singapore*

Zhimin Wang − *Division of Chemistry and Biological Chemistry, School of Physical & Mathematical Sciences, Nanyang Technological University, Singapore 637371 Singapore*

Ming Hu − *Division of Chemistry and Biological Chemistry, School of Physical & Mathematical Sciences, Nanyang Technological University, Singapore 637371 Singapore*

Qinyu Han − *Division of Chemistry and Biological Chemistry, School of Physical & Mathematical Sciences, Nanyang Technological University, Singapore 637371 Singapore*

Complete contact information is available at:
https://pubs.acs.org/10.1021/acsnano.0c00951

Notes

The authors declare no competing financial interest.

ACKNOWLEDGMENTS

(M408110000, M4082392.110.500000) in Nanyang Technological University (NTU).

REFERENCES

(1) Galluzzi, L.; Bravo-San Pedro, J. M.; Kroemer, G. Organelle-Specific Initiation of Cell Death. *Nat. Cell Biol.* **2014**, *16*, 728.

(2) Lundberg, E.; Borner, G. H. Spatial Proteomics: A Powerful Discovery Tool for Cell Biology. *Nat. Rev. Mol. Cell Biol.* **2019**, *20*, 285−302.

(3) Ali, M. R.; Wu, Y.; Tang, Y.; Xiao, H.; Chen, K.; Han, T.; Fang, N.; Wu, R.; El-Sayed, M. A. Targeting Cancer Cell Integrins Using Gold Nanorods in Photothermal Therapy Inhibits Migration through Affecting Cytoskeletal Proteins. *Proc. Natl. Acad. Sci. U. S. A.* **2017**, *114*, E5655−E5663.

(4) Lyu, Y.; Cui, D.; Sun, H.; Miao, Y.; Duan, H.; Pu, K. Dendronized Semiconducting Polymer as Photothermal Nanocarrier for Remote Activation of Gene Expression. *Angew. Chem., Int. Ed.* **2017**, *56*, 9155−9159.

(5) Feng, Z.; Wang, H.; Wang, S.; Zhang, Q.; Zhang, X.; Rodal, A. A.; Xu, B. Enzymatic Assemblies Disrupt the Membrane and Target Endoplasmic Reticulum for Selective Cancer Cell Death. *J. Am. Chem. Soc.* **2018**, *140*, 9566−9573.

(6) Zhu, H.; Fan, J.; Du, J.; Peng, X. Fluorescent Probes for Sensing and Imaging within Specific Cellular Organelles. *Acc. Chem. Res.* **2016**, *49*, 2115−2126.

(7) Ma, X.; Gong, N.; Zhong, L.; Sun, J.; Liang, X.-J. Future of Nanotherapeutics: Targeting the Cellular Sub-Organelles. *Biomaterials* **2016**, *97*, 10−21.

(8) Wang, H.; Feng, Z.; Wang, Y.; Zhou, R.; Yang, Z.; Xu, B. Integrating Enzymatic Self-Assembly and Mitochondria Targeting for Selectively Killing Cancer Cells without Acquired Drug Resistance. *J. Am. Chem. Soc.* **2016**, *138*, 16046−16055.

(9) Chen, H.; Wang, J.; Feng, X.; Zhu, M.; Hoffmann, S.; Hsu, A.; Qian, K.; Huang, D.; Zhao, F.; Liu, W. Mitochondria-Targeting Fluorescent Molecules for High Efficiency Cancer Growth Inhibition and Imaging. *Chem. Sci.* **2019**, *10*, 7946−7951.

(10) Ai, X.; Lyu, L.; Zhang, Y.; Tang, Y.; Mu, J.; Liu, F.; Zhou, Y.; Zuo, Z.; Liu, G.; Xing, B. Remote Regulation of Membrane Channel Activity by Site-Specific Localization of Lanthanide-Doped Upconversion Nanocrystals. *Angew. Chem., Int. Ed.* **2017**, *56*, 3031−3035.

(11) Gao, W.; Li, S.; Liu, Z.; Sun, Y.; Cao, W.; Tong, L.; Cui, G.; Tang, B. Targeting and Destroying Tumor Vasculature with a Near-Infrared Laser-Activated "Nanobomb" for Efficient Tumor Ablation. *Biomaterials* **2017**, *139*, 1−11.

(12) Zhang, R.; Cheng, K.; Antaris, A. L.; Ma, X.; Yang, M.; Ramakrishnan, S.; Liu, G.; Lu, A.; Dai, H.; Tian, M. Hybrid Anisotropic Nanostructures for Dual-Modal Cancer Imaging and Image-Guided Chemo-Thermo Therapies. *Biomaterials* **2016**, *103*, 265−277.

(13) Yu, N.; Huang, L.; Zhou, Y.; Xue, T.; Chen, Z.; Han, G. Near-Infrared-Light Activatable Nanoparticles for Deep-Tissue-Penetrating Wireless Optogenetics. *Adv. Healthcare Mater.* **2019**, *8*, 1801132.

(14) Huang, X.; El-Sayed, I. H.; Qian, W.; El-Sayed, M. A. Cancer Cell Imaging and Photothermal Therapy in the Near-Infrared Region by Using Gold Nanorods. *J. Am. Chem. Soc.* **2006**, *128*, 2115−2120.

(15) Chan, M.-H.; Chen, S.-P.; Chen, C.-W.; Chan, Y.-C.; Lin, R. J.; Tsai, D. P.; Hsiao, M.; Chung, R.-J.; Chen, X.; Liu, R.-S. Single 808 nm Laser Treatment Comprising Photothermal and Photodynamic Therapies by Using Gold Nanorods Hybrid Upconversion Particles. *J. Phys. Chem. C* **2018**, *122*, 2402−2412.

(16) Wang, Z.; Zhen, X.; Upputuri, P. K.; Jiang, Y.; Lau, J.; Pramanik, M.; Pu, K.; Xing, B. Redox-Activatable and Acid-Enhanced Nanotheranostics for Second Near-Infrared Photoacoustic Tomography and Combined Photothermal Tumor Therapy. *ACS Nano* **2019**, *13* (5), 5816−5825.

(17) Chan, M. H.; Pan, Y. T.; Lee, I. J.; Chen, C. W.; Chan, Y. C.; Hsiao, M.; Wang, F.; Sun, L.; Chen, X.; Liu, R. S. Minimizing the Heat Effect of Photodynamic Therapy Based on Inorganic Nano-composites Mediated by 808 nm Near-Infrared Light. *Small* **2017**, *13*, 1700038.

(18) Liu, G.; Zhu, J.; Guo, H.; Sun, A.; Chen, P.; Xi, L.; Huang, W.; Song, X.; Dong, X. Mo$_2$C-Derived Polyoxometalate for NIR-II Photoacoustic Imaging-Guided Chemodynamic/Photothermal Synergistic Therapy. *Angew. Chem., Int. Ed.* **2019**, *58*, 18641−18646.

(19) Dong, Q.; Wang, X.; Hu, X.; Xiao, L.; Zhang, L.; Song, L.; Xu, M.; Zou, Y.; Chen, L.; Chen, Z.; Tan, W. Simultaneous Application of Photothermal Therapy and an Anti-Inflammatory Prodrug Using Pyrene-Aspirin-Loaded Gold Nanorod Graphitic Nanocapsules. *Angew. Chem., Int. Ed.* **2018**, *57*, 177−181.

(20) Ng, K.; Takada, M.; Cheng, C. S.; Zheng, G. Self-Sensing Porphysomes for Fluorescence-Guided Photothermal Therapy. *Bioconjugate Chem.* **2015**, *26*, 345−351.

(21) Valcourt, D. M.; Dang, M. N.; Day, E. S. IR820-Loaded PLGA Nanoparticles for Photothermal Therapy of Triple-Negative Breast Cancer. *J. Biomed. Mater. Res., Part A* **2019**, *107*, 1702−1712.

(22) Feng, W.; Han, X.; Wang, R.; Gao, X.; Hu, P.; Yue, W.; Chen, Y.; Shi, J. Nanocatalysts-Augmented and Photothermal-Enhanced Tumor-Specific Sequential Nanocatalytic Therapy in Both NIR-I and NIR-II Biowindows. *Adv. Mater.* **2018**, *31*, 1805919.

(23) Yuan, H.; Fales, A. M.; Vo-Dinh, T. TAT Peptide-Functionalized Gold Nanostars: Enhanced Intracellular Delivery and Efficient NIR Photothermal Therapy Using Ultralow Irradiance. *J. Am. Chem. Soc.* **2012**, *134*, 11358−11361.

(24) Delbecq, S. P.; Rosenbaum, J. C.; Klevit, R. E. A Mechanism of Subunit Recruitment in Human Small Heat Shock Protein Oligomers. *Biochemistry* **2015**, *54*, 4276−4284.

(25) Pérez-Hernández, M.; del Pino, P.; Mitchell, S. G.; Moros, M.; Stepien, G.; Pelaz, B.; Parak, W. J.; Gálvez, E. M.; Pardo, J.; de la Fuente, J. s. M. Dissecting the Molecular Mechanism of Apoptosis during Photothermal Therapy Using Gold Nanoprisms. *ACS Nano* **2015**, *9*, 52−61.

(26) Zhu, X.; Feng, W.; Chang, J.; Tan, Y.-W.; Li, J.; Chen, M.; Sun, Y.; Li, F. Temperature-Feedback Upconversion Nanocomposite for Accurate Photothermal Therapy at Facile Temperature. *Nat. Commun.* **2016**, *7*, 10437.

(27) Li, W.; Yang, J.; Luo, L.; Jiang, M.; Qin, B.; Yin, H.; Zhu, C.; Yuan, X.; Zhang, J.; Luo, Z. Targeting Photodynamic and Photothermal Therapy to the Endoplasmic Reticulum Enhances Immunogenic Cancer Cell Death. *Nat. Commun.* **2019**, *10*, 1−16.

(28) Li, N.; Sun, Q.; Yu, Z.; Gao, X.; Pan, W.; Wan, X.; Tang, B. Nuclear-Targeted Photothermal Therapy Prevents Cancer Recurrence with Near-Infrared Triggered Copper Sulfide Nanoparticles. *ACS Nano* **2018**, *12*, 5197−5206.

(29) Pramanik, S. K.; Sreedharan, S.; Singh, H.; Green, N. H.; Smythe, C.; Thomas, J. A.; Das, A. Imaging Cellular Trafficking Processes in Real Time Using Lysosome Targeted Up-Conversion Nanoparticles. *Chem. Commun.* **2017**, *53*, 12672−12675.

(30) Lu, S.; Tu, D.; Hu, P.; Xu, J.; Li, R.; Wang, M.; Chen, Z.; Huang, M.; Chen, X. Multifunctional Nano-Bioprobes Based on Rattle-Structured Upconverting Luminescent Nanoparticles. *Angew. Chem., Int. Ed.* **2015**, *54*, 7915−7919.

(31) Li, L. L.; Zhang, R.; Yin, L.; Zheng, K.; Qin, W.; Selvin, P. R.; Lu, Y. Biomimetic Surface Engineering of Lanthanide-Doped Upconversion Nanoparticles as Versatile Bioprobes. *Angew. Chem., Int. Ed.* **2012**, *51*, 6121−6125.

(32) Fan, W.; Bu, W.; Shi, J. On the Latest Three-Stage Development of Nanomedicines Based on Upconversion Nanoparticles. *Adv. Mater.* **2016**, *28*, 3987−4011.

(33) Li, W.; Wang, J.; Ren, J.; Qu, X. Near-Infrared Upconversion Controls Photocaged Cell Adhesion. *J. Am. Chem. Soc.* **2014**, *136*, 2248−2251.

(34) Liu, X.; Deng, R.; Zhang, Y.; Wang, Y.; Chang, H.; Huang, L.; Liu, X. Probing the Nature of Upconversion Nanocrystals: Instrumentation Matters. *Chem. Soc. Rev.* **2015**, *44*, 1479−1508.

(35) Yang, Y.; Aw, J.; Xing, B. Nanostructures for NIR Light-Controlled Therapies. *Nanoscale* **2017**, *9*, 3698−3718.

(36) Liu, F.; He, X.; Lei, Z.; Liu, L.; Zhang, J.; You, H.; Zhang, H.; Wang, Z. Facile Preparation of Doxorubicin-Loaded Upconversion@ Polydopamine Nanoplatforms for Simultaneous *In Vivo* Multimodality Imaging and Chemophotothermal Synergistic Therapy. *Adv. Healthcare Mater.* **2015**, *4*, 559−568.

(37) Xu, J.; Kuang, Y.; Lv, R.; Yang, P.; Li, C.; Bi, H.; Liu, B.; Yang, D.; Dai, Y.; Gai, S.; He, F.; Xing, B.; Lin, J. Charge Convertibility and Near Infrared Photon Co-Enhanced Cisplatin Chemotherapy Based on Upconversion Nanoplatform. *Biomaterials* **2017**, *130*, 42−55.

(38) Ai, X. Z.; Ho, C.; Aw, J.; Attia, A.; Mu, J.; Wang, Y.; Wang, X.; Wang, Y.; Liu, X.; Chen, H.; Gao, M.; Chen, X.; Yeow, E. K.; Liu, G.; Olivo, M.; Xing, B. *In Vivo* Covalent Cross-Linking of Photon-Converted Rare-Earth Nanostructures for Tumor Localization and Theranostics. *Nat. Commun.* **2016**, *7*, 10432.

(39) Zhang, Y.; Zhan, X.; Xiong, J.; Peng, S.; Huang, W.; Joshi, R.; Cai, Y.; Liu, Y.; Li, R.; Yuan, K. Te9mperature-Dependent Cell Death Patterns Induced by Functionalized Gold Nanoparticle Photothermal Therapy in Melanoma Cells. *Sci. Rep.* **2018**, *8*, 8720.

(40) Parsell, D.; Lindquist, S. The Function of Heat-Shock Proteins in Stress Tolerance: Degradation and Reactivation of Damaged Proteins. *Annu. Rev. Genet.* **1993**, *27*, 437−496.

(41) Åkerfelt, M.; Morimoto, R. I.; Sistonen, L. Heat Shock Factors: Integrators of Cell Stress, Development and Lifespan. *Nat. Rev. Mol. Cell Biol.* **2010**, *11*, 545.

(42) Nagy, E.; Balogi, Z.; Gombos, I.; Åkerfelt, M.; Björkbom, A.; Balogh, G.; Török, Z.; Maslyanko, A.; Fiszer-Kierzkowska, A.; Lisowska, K. Hyperfluidization-Coupled Membrane Microdomain Reorganization Is Linked to Activation of the Heat Shock Response in a Murine Melanoma Cell Line. *Proc. Natl. Acad. Sci. U. S. A.* **2007**, *104*, 7945−7950.

(43) Urban, P.; Kirchner, S. R.; Mühlbauer, C.; Lohmüller, T.; Feldmann, J. Reversible Control of Current across Lipid Membranes by Local Heating. *Sci. Rep.* **2016**, *6*, 22686.

(44) Palankar, R.; Pinchasik, B.-E.; Khlebtsov, B. N.; Kolesnikova, T. A.; Möhwald, H.; Winterhalter, M.; Skirtach, A. G. Nanoplasmonically-Induced Defects in Lipid Membrane Monitored by Ion Current: Transient Nanopores *versus* Membrane Rupture. *Nano Lett.* **2014**, *14*, 4273−4279.

(45) Koide, R.; Nishimura, S. I. Antiadhesive Nanosomes Facilitate Targeting of the Lysosomal GlcNAc Salvage Pathway through Derailed Cancer Endocytosis. *Angew. Chem.* **2019**, *131*, 14655−14660.

(46) Pérez-Hernández, M.; del Pino, P.; Mitchell, S. G.; Moros, M.; Stepien, G.; Pelaz, B.; Parak, W. J.; Gálvez, E. M.; Pardo, J.; de la Fuente, J. s. M. Dissecting the Molecular Mechanism of Apoptosis during Photothermal Therapy Using Gold Nanoprisms. *ACS Nano* **2015**, *9*, 52−61.

(47) Cirman, T.; Orešić, K.; Mazovec, G. D.; Turk, V.; Reed, J. C.; Myers, R. M.; Salvesen, G. S.; Turk, B. Selective Disruption of Lysosomes in HeLa Cells Triggers Apoptosis Mediated by Cleavage of Bid by Multiple Papain-Like Lysosomal Cathepsins. *J. Biol. Chem.* **2004**, *279*, 3578−3587.